

Microstructuring YbRh_2Si_2 for resistance and noise measurements down to ultra-low temperatures

Alexander Steppke^{1,2,3}, Sandra Hamann^{1,4}, Markus König¹,
 Andrew P. Mackenzie^{1,5}, Kristin Kliemt⁶, Cornelius Krellner⁶,
 Marvin Kopp⁶, Martin Lonsky⁶, Jens Müller⁶, Lev V. Levitin⁷,
 John Saunders⁷, Manuel Brandt¹

¹ Max-Planck-Institute for Chemical Physics of Solids, Noethnitzer Str. 40, 01187 Dresden, Germany

² University of Zurich, Winterthurerstr. 190, 8057 Zurich, Switzerland

³ Paul Scherrer Institute, Forschungsstr. 111, 5232 Villigen, Switzerland

⁴ Helmholtz-Zentrum Dresden-Rossendorf, Bautzner Landstr. 400, 01328 Dresden, Germany

⁵ Scottish Universities Physics Alliance, School of Physics and Astronomy, University of St Andrews, St Andrews, UK

⁶ Physikalisches Institut, Goethe-Universität Frankfurt, Max-von-Laue-Str. 1, 60438 Frankfurt am Main, Germany

⁷ Department of Physics, Royal Holloway University of London, Egham, Surrey TW20 0EX, UK

Abstract. The discovery of superconductivity in the quantum critical Kondo-lattice system YbRh_2Si_2 at an extremely low temperature of 2 mK has inspired efforts to perform high-resolution electrical resistivity measurements down to this temperature range in highly conductive materials. Here we show that control over the sample geometry by microstructuring using focused-ion-beam (FIB) techniques allows to reach ultra-low temperatures and increase signal-to-noise ratios (SNR) tenfold, without adverse effects to sample quality. In five experiments we show four-terminal sensing resistance and magnetoresistance measurements which exhibit sharp phase transitions at the Néel temperature, and Shubnikov-de-Haas (SdH) oscillations between 13 T and 18 T where we identified a new SdH frequency of 0.39 kT. The increased SNR allowed resistance fluctuation (noise) spectroscopy that would not be possible for bulk crystals, and confirmed intrinsic $1/f$ -type fluctuations. Under controlled strain, two thin microstructured samples exhibited a large increase of T_N from 67 mK up to 188 mK while still showing clear signatures of the phase transition and SdH oscillations. SQUID-based thermal noise spectroscopy measurements in a nuclear demagnetisation refrigerator down to 0.95 mK, show a sharp superconducting transition at $T_c = 1.2$ mK. These experiments demonstrate microstructuring as a powerful tool to investigate the resistance and the noise spectrum of highly conductive correlated metals over wide temperature ranges.

PACS numbers: 71.27.+a Strongly correlated electron systems; heavy fermions, 72.15.Eb Electrical and thermal conduction in crystalline metals and alloys, 05.40.-a Fluctuation phenomena, random processes, noise, and Brownian motion

1. Introduction

A temperature-dependent measurement of the resistivity of a material provides several insights into its physical properties. For instance, we can observe subtle changes in the electronic structure such as spin or charge density waves [1], structural phase transitions [2] and more dramatic changes such as superconductivity.

The development of lock-in amplifiers in the early 1950s [3] has simplified resistance measurements by extracting signals well below the noise floor [4], so that nowadays a measurement of the resistivity of very good metals has become standard practice [5]. Moreover, the temperature-dependent resistivity of particular materials allows their use as high-precision secondary thermometers [6], often over wide temperature ranges.

High-resolution resistance measurements can easily be performed under ambient conditions. However, at very low temperatures (milli- or microkelvins), a key limitation of standard four-terminal sensing techniques, with either voltage or current excitation, is the dissipation, which must be minimized. Otherwise, insufficient thermalization leads to temperature gradients or generally prevents cooling to lowest temperatures. Dissipation in the form of Joule heating is mainly caused by the electrical resistance of the contacts to the sample R_c and the sample's own resistance R_s , when driven by an either constant- or time varying excitation current I_{exc} .

We therefore need to find a balance in any low temperature resistance measurement between a sufficiently large measured sample voltage U_s and minimizing the dissipated power P_{diss} , which are given by

$$U_s = R_s \cdot I_{\text{exc}} \quad (1)$$

and

$$P_{\text{diss}} = (R_s + R_c) \cdot I_{\text{exc}}^2. \quad (2)$$

In many classes of correlated materials, e.g. oxides such as the cuprate superconductors, R_c can be higher than several ohms and, even for metallic samples, can reach hundreds of milliohms, exceeding R_s and dominating the dissipation.

A straightforward approach to this optimization problem is to reduce I_{exc} , thereby exploiting the quadratic dependence in the dissipated power. Addressing the corresponding reduction in signal amplitude led to the development of a wide range of techniques. These range from electrical circuits using a bridge-type setup, which were crucial for the discovery of superconductivity [7], over the aforementioned lock-in amplifiers to amplification techniques involving low-temperature transformers [8] or advanced superconducting quantum interference device (SQUID) amplifiers [9].

Still, there is a limit to this approach, especially when measuring metallic samples with high conductivity. The reduction in signal amplitude by reducing the excitation current produces a setup which is susceptible to any external electrical disturbances. In addition, the smaller signal leads to a decrease in resolution, which can make the extraction of features such as quantum oscillations or topological transitions infeasible.

With modern microstructuring techniques, a new and different path opens up to address this trade-off between dissipation and achievable resolution. With precision control over the sample geometry, one can increase the ohmic resistance R_s by creating thin bar-shaped or meander-like samples. We will show that it is possible to increase R_s by a factor 250 (up to some Ω) while keeping R_c small (a few $\text{m}\Omega$). We can then distinguish two regimes in the measured signal amplitude

$$U_{\text{signal}} = \sqrt{\frac{R_s^2 P_{\text{diss}}}{R_s + R_c}} \quad (3)$$

for a given fixed maximum dissipation. For $R_s \ll R_c$, an increase in R_s is directly proportional to the amplitude and for higher R_s , we observe a square-root increase of the amplitude. The assumption of a fixed maximum dissipation is often fulfilled when the sample is thermally strongly linked to its environment. Here lies also the limitation of this approach. For extreme changes in the geometry, one can reduce the thermal coupling between sample and cold bath significantly. Under these semi-adiabatic conditions, the decrease in thermal conductance to the cold bath outweighs the reduced dissipation.

From these considerations we can devise an optimum geometry starting from a irregularly shaped bulk sample with approximate cross section area A and length l . The heat capacity of such a sample is then given by $C = c \rho_m A l$ with the density ρ_m and the specific heat c . If possible, we do not want to decrease the heat capacity but only increase the resistance given by $R_s = \rho l/A$. This can be achieved by cutting thin slots, creating a meander-like structure as shown in figure 1(a). Even by cutting only a single narrow slot ($A \rightarrow A/2, l \rightarrow 2l$) into a rectangular sample, one can leave C almost unchanged while increasing the resistance fourfold.

Whereas these considerations were focused on a resistance measurement using a four-terminal technique, alternative approaches can also benefit from the same structuring technique. For measurements at lowest possible temperatures, a further decrease in dissipation can be achieved by removing the drive current completely and deducing the resistance from the sample's Johnson noise. Due to the small size of this effect ($\ll 10^{-9}$ V at 10 mK), very high amplification is required, which can be achieved by inductive coupling to a SQUID [10, 11, 12]. Although this technique has been optimized by using modern SQUIDS [9] and new circuit designs [13], so that the resistance of the sample itself can be of the order of 0.1 – 1 $\text{m}\Omega$, inherently the circuit loop includes the contact resistances in series with the sample's own resistance. In practice, for bonded or spot-welded contacts with small wires (25-50 μm in diameter), this can also be of the order of 0.1 to 1 $\text{m}\Omega$, but in many cases still much larger than that of samples from highly conductive materials. Therefore, a higher sample resistance can be beneficial for a wide range of techniques, and we outline several ways this can be achieved by changing the geometry using microstructuring.

In single crystals of highly conductive materials with $\rho_0 \leq 1 \mu\Omega\text{cm}$, an increase of the resistance is difficult to achieve with standard sample preparation techniques, even for a modest resistance of $R_s = 0.1 \Omega$. We would need to cut a sample so that the length to cross-sectional-area ratio l/A reaches 10^5 cm^{-1} to achieve a resistance comparable to

the contact resistance. This means that even if the growth of large crystals with $l \approx 1$ cm is feasible, the cross-sectional-area needs to be of the order of $1000 \mu\text{ m}^2$. Assuming that the sample's width could be cut to $100 \mu\text{ m}$, its thickness has to be reduced to $10 \mu\text{ m}$, which is difficult to achieve and even more difficult to handle manually. These established sample preparation techniques, e.g. using diamond wire saws, polishing and lapping, are therefore not suitable, and more complex geometries like a meander-shaped resistance track are required to achieve significant resistances increases.

In contrast to the aforementioned methods and other microstructuring techniques (see Appendix), the recent development and commercial availability of focused-ion-beam (FIB) devices (see also Appendix) allows such a sample manipulation. These devices can shape and contact samples on sub-micrometer dimensions without altering their physical properties [14]. Thin metallic platelets can be cut in long patterned meander tracks of width of less than $5 \mu\text{ m}$ [15] and along user-selected crystalline directions [16]. With a track width of $5 \mu\text{ m}$ and a typical thickness of $20 \mu\text{ m}$ for thin samples, $A = 10^{-6} \text{ cm}^2$, which in the corresponding example given above would result in $R = 1 \Omega$.

Such a strong increase in resistance allows resistivity measurements at much lower temperatures and higher signal-to-noise ratio (SNR), and therefore to access a wide range of phenomena such as superconductivity below 10 mK and voltage noise spectra at classical and quantum phase transitions, and to resolve subtle signatures, for example those caused by topological transitions [17].

Here we demonstrate this approach for the strongly correlated electron system YbRh_2Si_2 [18, 19, 20, 21], a canonical heavy-fermion (HF) compound. One of the main motivations for this work was the discovery of unconventional superconductivity (SC) in YbRh_2Si_2 [18, 22] at the very low critical temperature $T_c = 2 \text{ mK}$ [22]. Whereas this was demonstrated by ac-susceptibility measurements [22, 23], a resistivity measurement was deemed infeasible in as-grown crystals, as the dissipation is prohibitively high in a four-terminal measurement. Only recently, transport experiments in highly optimized setups [24, 25] corroborated the initial findings.

The discovery of superconductivity in YbRh_2Si_2 was unexpected because it is a rare phenomenon in Yb-based HF compounds, with $\beta\text{-YbAlB}_4$ ($T_c = 80 \text{ mK}$) [26] the only other known superconducting material in this class. On the other hand, there are many Ce-based (Ce is considered the electron analog of Yb) HF superconductors with critical temperatures as high as 2.3 K [27]. Whereas the particularities of the superconducting state in YbRh_2Si_2 are still under investigation, it has been suggested that the suppression of antiferromagnetic (AFM) order ($T_N = 70 \text{ mK}$ [18]) by nuclear ordering promotes the emergence of superconductivity [22, 23]. Such a concomitant suppression of magnetic order with the appearance of superconductivity spans wide ranges of material families beyond other HF systems [28, 29], to cuprates [30], pnictides or organic charge-transfer salts [31, 32]. If the mechanism behind HF superconductivity is connected to vanishing magnetic order, we can speculate that in Yb-based materials with their lower ordering temperatures, SC also appears at much lower temperatures (in the mK range) compared to Ce-based compounds. A reliable way of measuring resistance at those temperatures

will therefore facilitate the discovery of more Yb-based superconductors. In addition, this enables measuring the intrinsic noise spectrum of a high-resistance sample of a material close to a classical or quantum phase transition, which can provide additional information about the critical fluctuations.

In the following we illustrate microstructuring approaches and their advantages in YbRh_2Si_2 , using electrical resistivity and noise measurements in five experiments from three meander-like and two bar-like samples:

- i Study of the resistivity exponent across T_N on meander #1
- ii Magnetoresistance and Shubnikov-de-Haas oscillations on meander #2
- iii High-temperature noise spectroscopy on meander #3
- iv Tuning of T_N by strain on meander #2, bar #1 and bar #1 after reprocessing
- v Ultra-low temperature noise measurements on meander #2

2. Study of the resistivity exponent across T_N on meander #1

For our first experiment, a flat, unpolished YbRh_2Si_2 crystal [33] with a size of approx. $1.8 \text{ mm} \times 1.2 \text{ mm}$ was fixed onto a Si substrate using Araldite Rapid. We then used a shadow-mask technique and standard electron-beam evaporation of Au to deposit contacts onto the YbRh_2Si_2 crystal and connect the crystal to Au leads and contact pads on the Si substrate. The FIB patterning of the crystal into the meander was done in a standard FIB/SEM system (FEI Helios Nanolab G3), using an acceleration voltage and Ga-ion beam current of 30 kV and 65 nA, respectively, for the initial steps. Lower values were used in subsequent steps to minimize the damage to the crystal. The meander structure, shown in figure 1(a), consists of 20 straight wire-like segments with dimensions of $L \times W \approx 900 \mu\text{m} \times 14 \mu\text{m}$ each, resulting in a total wire length of 18.8 mm including the bends connecting the straight segments, i.e. $l/W \approx 1250$. Due to the necessary large size of the initial bulk crystal the meander thickness varies between $15 \mu\text{m}$ and $75 \mu\text{m}$ (cf. Tab. 2).

Four-terminal resistivity measurements were performed using a Quantum Design PPMS from room temperature to 0.4 K and using an Oxford Instruments dilution refrigerator down to 20 mK equipped with low-temperature transformers [8].

Resistance measurements in the temperature range from 300 K to 30 mK before and after microstructuring are shown in Figure 1. Microstructuring led to an increase of the resistance by a factor of 250. Although the thickness of the sample is not uniform, we can estimate a geometry factor of $l/A = l/(d_{\text{mean}} \cdot W) = 18,800 \mu\text{m}/(45 \mu\text{m} \cdot 14 \mu\text{m}) = 630 \mu\text{m}^{-1}$. Both measurements can nearly be scaled on top of each other, although we observed some undesired parallel conductance path through the Si substrate near room temperature. They show the expected Kondo-lattice behavior with a coherence maximum at $T^* \approx 100 \text{ K}$ [18] and a strong drop for $T < T^*$ followed by the linear-in- T dependence of the resistivity at low temperatures (see figure 2(c)), characteristic of the quantum critical behavior of this material [19].

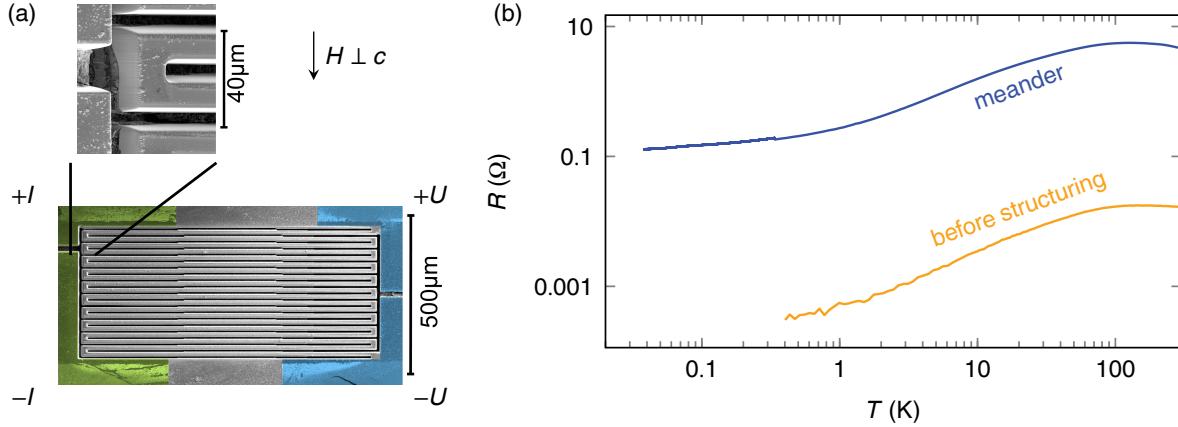


Figure 1. (a) Electron microscope image of the YbRh_2Si_2 meander #1. The four-terminal contacts for electrical measurements are shown in green (current) and blue (voltage). The meander is structured from the ab-plane of the crystal, the applied field direction is perpendicular to the long sides of the meander and perpendicular to the c-axis. (b) Temperature dependence of the resistance of the YbRh_2Si_2 sample before and after FIB structuring. The electrical contacts using bonded gold wires remained on the sample during microstructuring.

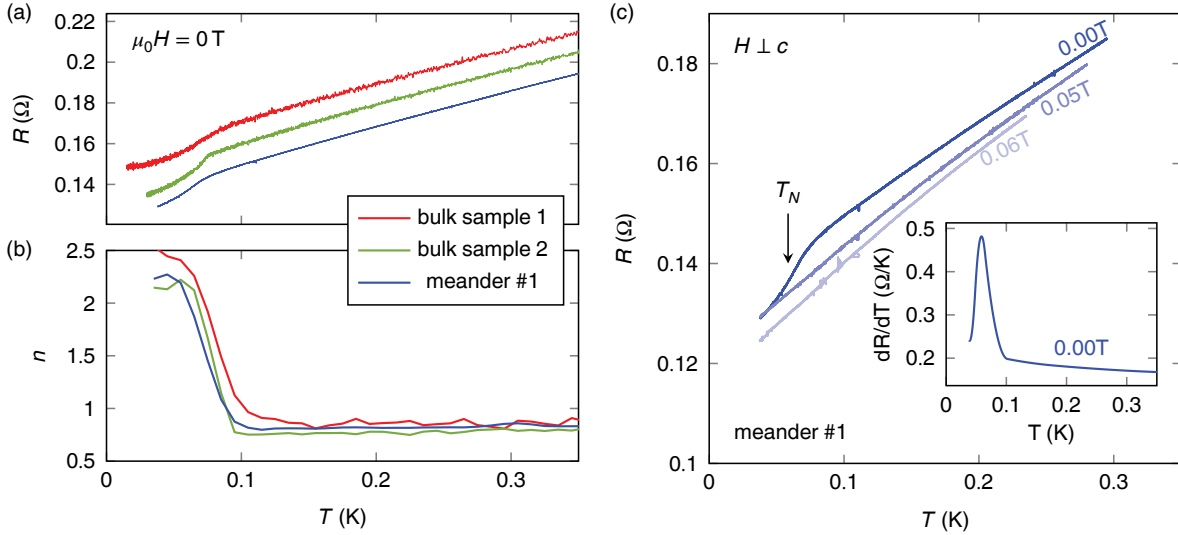


Figure 2. (a) Low-temperature electrical resistance R of the microstructured meander #1 at zero field. For comparison the electrical resistance of two bulk samples (sample 1 from Ref. [34] and sample 2 from Ref. [21]) are scaled on the meander #1 data and shifted subsequently with an offset of $+0.01 \Omega$ for clarity. (b) Resistance exponent n from the analysis with $R(T) = R_0 + A \cdot T^n$ above and within the AFM ordered phase. (c) Low temperature electrical resistance R of the microstructured meander #1 measured at different magnetic fields applied along the basal plane ($B \perp c$). Inset: Temperature derivative of the electrical resistance at zero field. The peak indicates $T_N = 67 \text{ mK}$, close to values reported for previous sample growths of 70 mK [35] and 72 mK [36].

We focus now on the low-temperature properties of meander #1 as shown in figure 2: A kink in the resistance is evidence of the onset of AFM ordering (figure 2(a),(c)). Comparable to former measurements on bulk samples T_N is approximately 67 mK [18, 19]. Applying a magnetic field of $B_N = 0.06$ T along the basal plane suppresses the AFM ordering completely (see figure 2(c)) [35, 36].

To visualize the improvement in the obtained SNR we compare measurements on our microstructured meander #1 with those on two bulk samples taken with higher excitation currents (cf. figure 2 and Tab. 1). Here the measured resistance fluctuations are approximately normally distributed and we define the SNR as $R_{T \rightarrow 0}/R_{rms}$, with $R_{T \rightarrow 0}$ the lowest measured resistance and R_{rms} being the root-mean square value of the deviation from a noise free measurement in the temperature range up to 0.8 K.

Bulk sample 1 (from Ref. [34]) is, with an RRR of 71, comparable to the sample we used in this study, whereas bulk sample 2 (from Ref. [21]) is of higher quality with RRR = 136. Because the resistivity of all three samples is linear-in- T for $T > T_N$ and with nearly identical slope, we can scale all resistances onto that of the structured meander #1 (figure 2a).

It can be immediately seen that the data for the meander sample exhibits a significantly lower noise level. Whereas at $T = 0.15$ K for bulk samples 1 and 2 the observed signal to noise ratio R_{rms}/R_0 is 0.45% and 0.48%, respectively, it decreases by a factor of 10 to $R_{rms}/R_0 = 0.047\%$ in the meander #1. Although, in comparison with bulk sample #2 a 50 times smaller excitation current was used in the meander structure, the SNR increases by one order of magnitude.

Table 1. Properties of samples used in figure 2: The RRR is defined as $\rho_{T=300\text{K}}/\rho_0$ with $\rho_{T=300\text{K}} = 75 \mu\Omega\text{cm}$ [37, 38]. Resistance noise is obtained from voltage noise and taking into account the amplification of the low temperature transformer (1:100) used in all measurements.

Sample	meander #1	Bulk 1 ([34])	Bulk 2 ([21])
RRR	35	71	136
Equivalent voltage noise at 0.15K ($\text{V}/\sqrt{\text{Hz}}$)	$1.1 \cdot 10^{-12}$	$8.8 \cdot 10^{-14}$	$3.3 \cdot 10^{-14}$
Resistance noise at 0.15K ($\Omega/\sqrt{\text{Hz}}$)	$1.1 \cdot 10^{-8}$	$1.8 \cdot 10^{-10}$	$6.6 \cdot 10^{-12}$
R_{rms}/R_0	0.047%	0.45%	0.48%
SNR	2142	222	208
Excitation current (μA)	1	5	50
ρ_0 ($\mu\Omega\text{cm}$)	–	1.05	0.55

The decrease in the observed relative resistance fluctuations R_{rms}/R_0 is not only useful in itself to detect subtle features in the $R(T)$ profile, but it can additionally be used in a more precise analysis of derived quantities. For instance, an important quantity in systems close to a QCP is the temperature dependence of the resistivity which provides information about the nature of the electron scattering [39, 19]. Typical

resistance $R(T)$ curves are analyzed according to the function $R(T) = R_0 + AT^n$, where R_0 is the residual resistance, A is a measure of the electron–electron scattering rate and n is the exponent that in the standard theory of metals - the Fermi-liquid theory - is expected to be equal to 2 [40]. The anomalous exponent $n \approx 1$ observed in YbRh_2Si_2 is strong evidence for the presence of quantum critical fluctuations and the existence of a new class of an electron fluid [19]. Therefore, such an analysis would strongly benefit from high-resolution raw data.

In figure 2(b) we show the temperature evolution of $n(T)$ obtained from a least-squares fit using the aforementioned $R(T)$ using a sliding window of 0.04 K. Here R_0 is determined from the temperature dependence below T_N and then kept fixed for higher T . In comparison between the bulk sample 1 and the microstructured sample we observe a decrease in the relative uncertainty of $\Delta n/n$ above 100 mK from 0.05 to 0.01.

3. Magnetoresistance and Shubnikov-de-Haas oscillations on meander #2

When applying magnetic fields beyond the suppression of the AFM order, i.e. $B > B_N$, several topological Lifshitz transitions have been reported in YbRh_2Si_2 in the field range up to 20 T [41, 42, 43, 44] with associated changes of the Fermi surface [41, 38, 45, 46]. Because of the low quality of the samples and the limited resolution of the measurements, only three Lifshitz transitions were first observed using combined thermopower and resistivity measurements [43, 47]. A more precise study on better crystals revealed the presence of 8 Lifshitz transitions for fields up to 13 T applied along the [110] direction [44, 46]. Furthermore, de Haas–Van-Alphen (dHvA) and Shubnikov–de-Haas (SdH) studies were able to detect parts of the predicted Fermi surface structure, but the limited number of observed frequencies do only partially correspond to theoretical predictions [48, 41, 38, 45, 49].

We performed magnetic field-dependent resistance measurements on a second meander structure cut from a high-quality crystal of $\text{RRR} = 270$ described in Tab. 2 as meander #2. The higher quality of this crystal was achieved by optimizing the temperature profile together with the crucible material in a new furnace [50]. It turned out, that shortening the growth time by about one third in comparison to Ref. [33] and changing the crucible material to graphite or glassy carbon lead to less contamination of the melt from the crucible, which was an issue in Al_2O_3 -based crucibles. The corresponding magnetoresistance is shown in figure 3(a). With the increase in crystal quality and measurement resolution we are able to observe signatures of several Lifshitz transitions up to 13 T at fields comparable with previous investigations [43, 44]. This supports that microstructuring neither decreased the quality of the crystal, nor significantly influenced its intrinsic properties. At the same time though the relatively strong mechanical contact to the substrate material leads to a strain effect due to the differential thermal contraction as discussed below (see section 5).

Further evidence of the quality of the meander #2 is the presence of SdH oscillations at field above 10 T shown in figure 3(b). The observed frequencies of 2.55 kT,

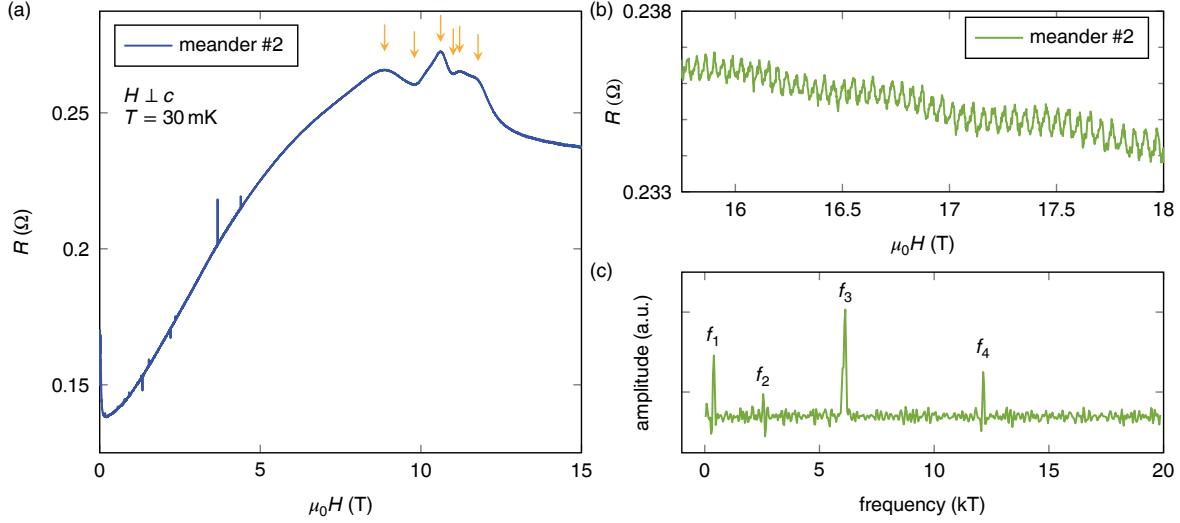


Figure 3. (a) Magnetoresistance of YbRh_2Si_2 measured on meander #2. There are several sharp slope changes which indicate Lifshitz transitions [43, 44]. In the field range up to 15 T at least six can be detected, indicated here by orange arrows. (b) SdH oscillations measured on meander #2 at a temperature of 30 mK. (c) Fourier transform of the magnetoresistance signal in high-field range field range between 11 T and 18 T. In this range strongest observed frequencies are located at 0.39 kT, 2.55 kT, 6.12 kT, and 12.15 kT.

6.12 kT and 12.15 kT (figure 3(c)) are in agreement with previously observed groups of frequencies in YbRh_2Si_2 attributed to the "doughnut" or "jungle-gym" sheets of the Fermi surface [42, 41, 38, 45]. The ab -plane orientation was not independently measured, although the values as high as 12.15 kT - similar to previous observations up to ≈ 14 kT for $B \parallel [110]$ [38, 45, 49] - suggest that the field in our sample was oriented close to the [110] direction. Furthermore, the positions of the kinks in magnetoresistance (orange arrows in figure 3) correspond well to those seen in Ref. [44] for $B \parallel [110]$. We additionally observe a low-frequency oscillation at 0.39 kT which has never been observed before. A similar frequency has been found experimentally only in the non-magnetic reference compound LuRh_2Si_2 and attributed to a beat frequency associated with the "jungle-gym" sheet of the Fermi surface [49], but the fundamental frequencies are not observed here. Renormalized band structure calculations show that the relevant states are minority states forming the "jungle-gym" Fermi surface sheet. They are strongly hybridized and are responsible for the topological transitions between 9 and 13 T in which, eventually, small portions of the Fermi surface disappear [43, 44]. So, the appearance of this new frequency at high fields corroborates the significant change of the topology of the Fermi surface and the difference to the low-field Kondo-lattice state [51].

4. High-temperature noise spectroscopy on meander #3

The control of the sample geometry and therefore its absolute resistance allows to observe not only the resistance in greater detail, but also resistance *fluctuations*. These fluctuations – measured as the noise power spectral density (PSD) S_R – reveal valuable information about the low-frequency charge carrier dynamics, which usually remains hidden in the averaged DC resistance R . In a voltage measurement $V = RI$ for a given current I , the PSD is defined as

$$S_V(f) = 2 \lim_{T_i \rightarrow \infty} \frac{1}{T_i} \left| \int_{-T_i/2}^{T_i/2} \delta V(t) e^{-i2\pi ft} dt \right|^2 \quad (4)$$

where $\delta V(t) = V(t) - \langle V(t) \rangle_t$ denotes the deviation of the signal from its long-term mean value and T_i the time interval of the measurement. Note that the time-averaged mean $\langle V(t) \rangle_t$ may be considered zero. Indeed, in the experiment, this 'DC-offset' often is sought to be suppressed in a five-terminal experimental setup so that only the fluctuating part of the signal is amplified and analyzed, see below. Averaging over the measuring time T_i determines the bandwidth of the measurement, where the low-frequency limit depends on the stability of the system and the patience of the experimenter.) It is $S_R = S_V/I^2$, and very often a $1/f$ -type noise $S_R \propto 1/f^\alpha$ with a frequency exponent $\alpha \approx 1$ is observed [52]. The *Wiener-Khintchine theorem* connects the autocorrelation function of the system, *i.e.* $\Psi(\tau) = \langle \delta V(t) \cdot \delta V(t+\tau) \rangle$, which characterizes the kinetics of the fluctuations and describes the charge carrier dynamics of condensed-matter system on the microscopic level, to the noise PSD:

$$S_V(f) = 4 \int_0^\infty \Psi(\tau) \cos(2\pi f\tau) d\tau. \quad (5)$$

By inverting the Fourier transform, the autocorrelation function $\Psi(\tau)$ can, in principle, be deduced from measuring $S_V(f)$. For zero delay ($\tau = 0$) the autocorrelation function equals the variance of the signal $\sigma^2 \equiv \Psi(0) = \int_0^\infty S_V(f) df = \langle \delta V(t)^2 \rangle$. Furthermore – unlike the linear (ohmic) part of the DC resistance, which measures the second moment of the current distribution in a sample – resistance fluctuations measure the fourth moment and hence are highly sensitive to local variations of electric fields and the current density [53].

Besides measurements of the thermal (Johnson) noise, which — by exploiting the Nyquist theorem — is an elegant way to determine the absolute resistance without driving a current through the sample, see section 6 below, structuring of YbRh_2Si_2 on the micrometer scale allows to detect another type of noise, namely the intrinsic $1/f$ -type fluctuations of a sample. Whereas thermal noise is frequency independent ('white') and therefore entirely uncorrelated, the $1/f^\alpha$ noise with a frequency exponent α close to 1 (in most cases between 0.8 and 1.4) reflects the kinetics of the charge fluctuations and therefore enables to access the microscopic motion and transitions of particles and their coupling to magnetic, structural or other degrees of freedom [53]. A power spectral density (PSD) $S \propto 1/f$ is ubiquitous in nature and is found in many condensed-matter systems like semiconductors and devices, metals and insulators, granular systems,

magnetic thin films and sensors, tunnel junctions, spin glasses, superconductors, colossal magnetoresistance materials etc, reflecting the low-frequency dynamics of charge carriers [54, 55, 52].

In correlated electron systems, percolative superconductivity in the coexistence region of antiferromagnetic insulating and superconducting phases [56], the critical slowing down of the charge carrier dynamics at the critical endpoint of a Mott transition [57], or the formation of a newly-discovered charge-glass state [58, 59] have been investigated using $1/f$ -noise spectroscopy, to name only a few examples. In the wide class of HF compounds, however, to the best of our knowledge so far no systematic measurements of this kind have been performed. For example, possible fluctuations coupled to the heavy quasiparticles upon entering the superconducting phase or at the Kondo temperature, and measurements of the intrinsic fluctuations in the vicinity of a quantum critical point seem attractive to explore. To a large part, the lack of such experiments in high-quality samples is due to the general difficulty to observe the intrinsic resistance fluctuations in highly-conductive systems, since the resistance noise PSD, S_R , scales with R^2 , i.e. for samples with a low absolute resistance R , the noise PSD S_R may be below the noise floor of the experimental setup. Considering a sample with active length ℓ and cross section A and Hooge's empirical law [60]

$$S_R = \gamma_H \frac{R^2}{n_c \Omega f} = \gamma_H \frac{\rho^2}{n_c f} \cdot \frac{\ell}{A^3}, \quad (6)$$

where γ_H denotes a material parameter characterizing the magnitude of the fluctuations of a system, n_c the charge carrier density, Ω the sample volume under investigation, and the resistivity ρ . Clearly, the geometry factor ℓ/A^3 , and therefore the signal to be measured, can be easily enhanced by a factor 10 to 100 in a meander structure as compared to a regular-shaped sample, thereby making $1/f$ -noise spectroscopy feasible in materials where it would not be for bulk crystals.

Besides enhancing the absolute resistance, the microstructuring of a sample allows to make use of a particular electronic circuit with which in an AC (lock-in) measurement the sample's resistance fluctuations can be shifted above the noise floor, often determined by the preamplifier [61]. Figure 4 depicts such a five-terminal setup, where the sample itself (meander #3, from same growth as meander #2) forms part of a Wheatstone bridge, thereby allowing to balance the DC offset such that only the fluctuating part of the signal is amplified and any perturbations as, e.g., thermoelectric effects, fluctuations of the voltage or current source and those of the thermal bath temperature are efficiently suppressed [61].

Figure 5(a) shows the voltage noise PSD of a microstructured meander sample YbRh_2Si_2 at $T = 20$ K for various applied currents measured in the above described five-terminal setup using a homemade resistance bridge, a voltage preamplifier SR554 and a lock-in amplifier SR830. Shown is the averaged voltage noise PSD calculated by a signal analyzer SR785, where typically 30 - 50 averages are sufficient. For low currents, a nearly frequency-independent behavior determined by the noise floor of the electronic setup is found. Clearly, S_V increases with increasing current and for larger currents a

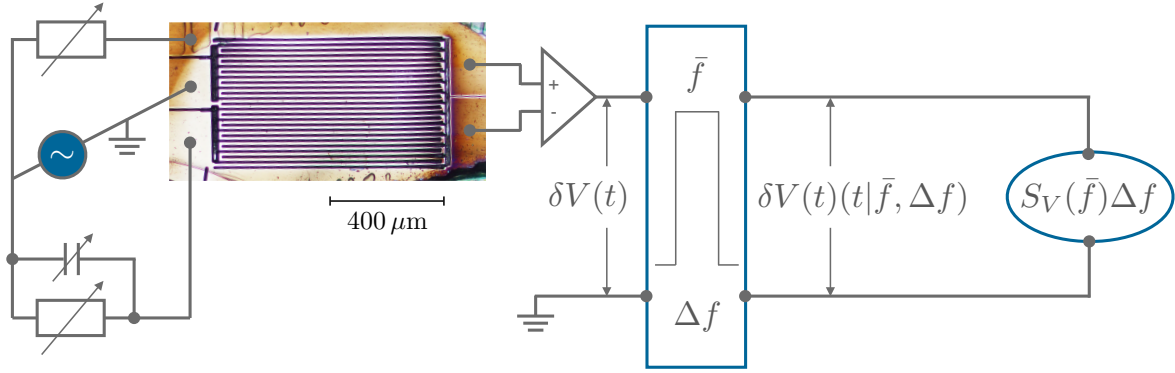


Figure 4. Schematic of the experimental five-point setup for low-level noise measurements on meander #3. On the input side (left) the balance circuit of the Wheatstone bridge is depicted with the middle contact of the sample's meander structure providing almost perfect symmetry of the two arms being part of the bridge. On the output side, only the fluctuating part of the voltage signal is first amplified, then processed by a band-pass adjustable-frequency filter with narrow bandwidth and an output detector that responds to the mean square of the signal (after [53]). In practice, noise sidebands produced by the resistance fluctuations that modulate the sinusoidally excited carriers are demodulated by a phase-sensitive detector (lock-in amplifier). The output signal of the lock-in amplifier is then processed by a spectrum analyzer which calculates the spectral density of the voltage fluctuations [61, 53, 55].

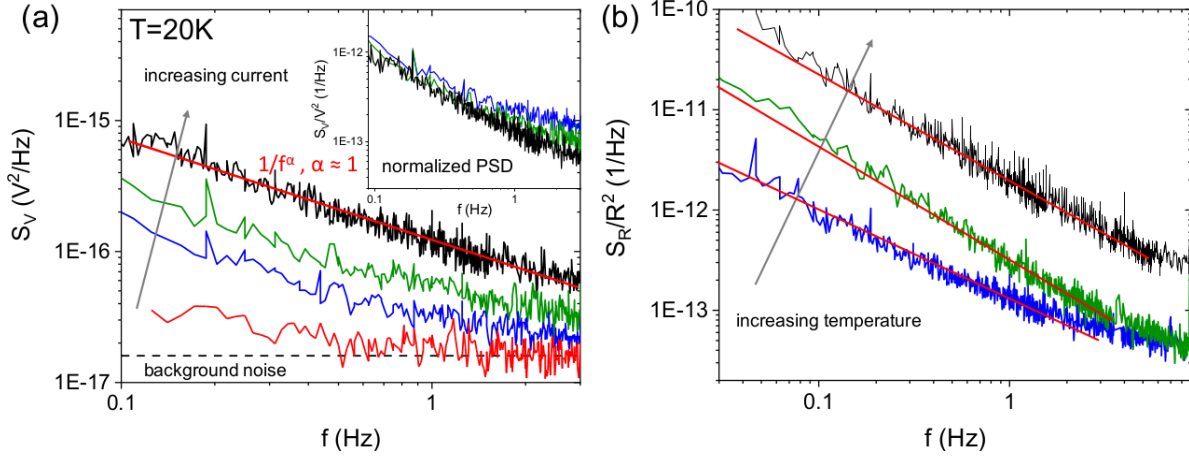


Figure 5. (a) Voltage noise PSD $S_V(f)$ at $T = 20\text{ K}$ for increasing currents from $I = 175\ \mu\text{A}$ (red) up to $I = 880\ \mu\text{A}$ (black) in a log-log representation showing an almost ‘white’ noise for low currents and a $1/f$ behavior for higher currents which scales with the square of the current as shown in the inset (see text). (b) Normalized PSD S_R/R^2 at three different temperatures ($T = 20\text{ K}, 75\text{ K}, 110\text{ K}$) demonstrating changes both in the noise PSD magnitude and the frequency exponent (slope).

distinct $1/f$ -type behavior $S_V \propto 1/f^\alpha$ with $\alpha \approx 1$ is observed. The inset shows the expected scaling $S_V \propto V^2 \propto I^2$ which is a main condition necessary to prove that $1/f$ -type fluctuations intrinsic to the sample resistance are observed, besides other checks to exclude the influence of spurious noise sources [55]. Figure 5(b) shows the normalized

resistance noise $S_R/R^2 = S_V/(I^2 \cdot R^2)$ for different temperatures demonstrating that temperature-dependent measurements showing variations of the intrinsic $1/f$ -type fluctuations, which reflect changes in the low-frequency charge carrier dynamics, are feasible in metallic HF compounds with low impedances. For the present sample, we estimate a Hooge parameter γ_H in Eq. (6) of order 10^5 using an estimated sample volume of $\Omega = 4.68 \cdot 10^{-12} \text{ m}^{-3}$ and a charge carrier density $n_c = 2.6 \cdot 10^{28} \text{ m}^{-3}$, see Ref.[62]. The relative $1/f$ -noise level of YbRh_2Si_2 estimated in this way is quite large compared to, e.g., clean and homogeneous semiconductors with typical values $\gamma_H \sim 10^{-3} - 10^{-2}$. However, γ_H in different materials has been found to vary over many orders of magnitude from 10^{-6} to 10^7 [54]. It should be noted, however, that the assumption of $1/f$ - noise being composed of independent fluctuation processes of individual mobile charge carriers in many cases is a crude oversimplification, see Ref.[52] and references therein. Therefore, the physical meaning of γ_H as introduced above is limited, in particular since the noise magnitude usually is strongly temperature dependent. However, it is still useful to compare the relative noise level of different compounds or different samples of the same compound via the parameter γ_H , which may serve as an additional parameter to characterize a sample. Furthermore, the temperature dependence of the noise magnitude $S_R/R^2(f)$, often conveniently determined at $f = 1 \text{ Hz}$, and the frequency exponent $\alpha = -\partial \ln S_R/R^2 / \partial \ln f$ provide information on the distribution and shift of spectral weight as a function of temperature of the low-frequency (collective) excitations. An analysis of the temperature dependence of γ_H and α will be published elsewhere. In this work we demonstrate that such measurements are feasible for high-quality low-impedance HF compounds.

5. Tuning of T_N by strain on meander #2 and bar #1

Control over sample geometry opens up further possibilities besides the improvement in the observed signal or its fluctuations. One of these is tuning of interactions through the application of strain from a substrate, either uni- or biaxially. This has been shown to influence the superconducting transition temperature in CeIrIn_5 [63] and can in general be used to shift phase transitions of hard [64] and soft [2] correlated electron systems. With YbRh_2Si_2 being located in the close vicinity of a QCP we report here on the first attempts to use this parameter to influence its Néel transition temperature. We expect that any positive uniaxial pressure independent of its direction will increase T_N because the discontinuities in the thermal expansion coefficient at T_N of YbRh_2Si_2 exhibit positive jumps for both the basal plane (\perp) and the c -axis (\parallel) [65]. With their magnitudes $\Delta\alpha_{\perp} = (9.8 \pm 0.5) \times 10^{-6} \text{ K}^{-1}$, $\Delta\alpha_{\parallel} = (6.5 \pm 0.5) \times 10^{-6} \text{ K}^{-1}$, we use an Ehrenfest relation

$$2 \frac{dT_N}{dp_{\perp}} + \frac{dT_N}{dp_{\parallel}} = \frac{dT_N}{dp} = \frac{T_N V_{\text{mol}}}{\Delta C} (2\Delta\alpha_{\perp} + \Delta\alpha_{\parallel}) \quad (7)$$

to estimate the response to pressure along the different directions. Here, with $\Delta C \approx 0.24 \text{ J/molK}$ [19], the pressure dependence of T_N at $p = 0$ is $dT_N/dp \approx$

0.36 K/GPa which slightly overestimates the response observed in hydrostatic pressure experiments [66] (see figure 6(b)).

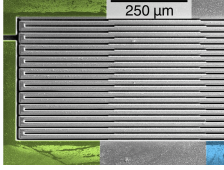
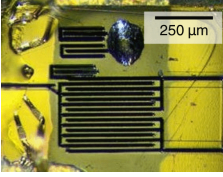
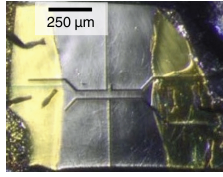
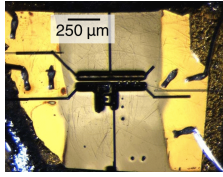
We observe indeed a significant shift of T_N in meander #2 which was used for the experiments shown in figures 3 and 7. It was cut from a high-quality sample with an RRR of 270 which grew in the shape of a thin platelet. This platelet was then glued to a silver sample holder using a thin layer of Stycast 1266 epoxy and cured at 60 °C (see Tab. 2). The relatively stiff epoxy (Young's modulus of 11 GPa at 77 K [67]), applied in a thin layer with a thickness of less than 100 μm leads to a significant transmission of the differential thermal contraction between the sample and the silver sample holder. This strain - which in this sample geometry is primarily uniaxial - leads to an increase of T_N from 67 mK to 120 mK in meander #2 (figure 6(b) and 7(b)). Such a shift of T_N was not found in the meander #1 which was attached to the substrate with a softer epoxy (Araldite Rapid).

We now estimate the magnitude of the shift in comparison with the differential thermal contraction through the substrate. As an estimate for the transmitted strain we can consider the thermal contraction of the silver substrate from room temperature to cryogenic temperatures of $\Delta L(T \rightarrow 0)/L \approx -0.4\%$ [6]. For YbRh_2Si_2 no complete data of thermal expansion from room temperature to low temperatures are available. From powder X-ray diffraction measurements down to 40 K the contraction in the ab -plane $\Delta a(T \rightarrow 0)/a$ is at least -0.08% . An alternative estimate can also be obtained by averaging values among similar systems (CeAl_3 , $\text{YbNi}_2\text{B}_2\text{C}$, YbAlB_4) found in literature. The mean of their volume thermal expansion coefficient β between 0 and 300 K is $5 \times 10^{-6} \text{ K}^{-1}$ ($\Delta L(T \rightarrow 0)/L \approx -0.15\%$) [68, 69, 70].

This results in a net compressive strain ϵ_0 between -0.25% and -0.32% for a thin microstructured sample of YbRh_2Si_2 attached with stiff epoxy to a silver substrate. In practice the strain transmission with such a meander-shaped sample geometry is limited by details of the interface epoxy between the sample and the substrate. Especially for thicker epoxy layers the transmitted strain decreases substantially and we expect that only thin samples approach this upper bound.

One technique to increase the transmitted strain is a sample geometry consisting of a long bar with large taps at each side (see Tab. 2). In such an optimized geometry a significant amount of force is transmitted through the taps at the side with much larger contact area to the substrate than through the bottom of the bar alone [64]. Additionally we used a filled epoxy, Stycast 2850, which further strengthens the mechanical interface between sample and substrate. Here the increase of the Néel temperature is highest in this sample with $T_N \approx 188 \text{ mK}$ (see figure 6). To distinguish the strain contribution from the interface at the bottom of the bar and from the side taps we performed another FIB procedure and removed the Stycast layer underneath the bar up to the taps. After this step T_N is reduced to 144 mK, reducing the strain transmission to the underside of the bar, which supports the dominant transmission via the outer taps in accordance with finite element simulations of such geometries [64]. A summary of parameters of the four microstructured samples is given in Tab. 2.

Table 2. Overview over various properties of the microstructured samples. Meander #1 is from an earlier growth using Al_2O_3 crucibles, meander #2, and bar #1 are from an optimized growth approach [50].

Sample	meander #1	meander #2	bar #1	bar #1 re-processed
RRR	35	270	180	180
Epoxy used	Araldite Rapid	Stycast 1266	Stycast 2850	partially removed
Thickness	15-75 μm	10 μm	10 μm	10 μm
Shape	meander	meander	bar	bar
T_N	67 mK	120 mK	188 mK	144 mK
Image				

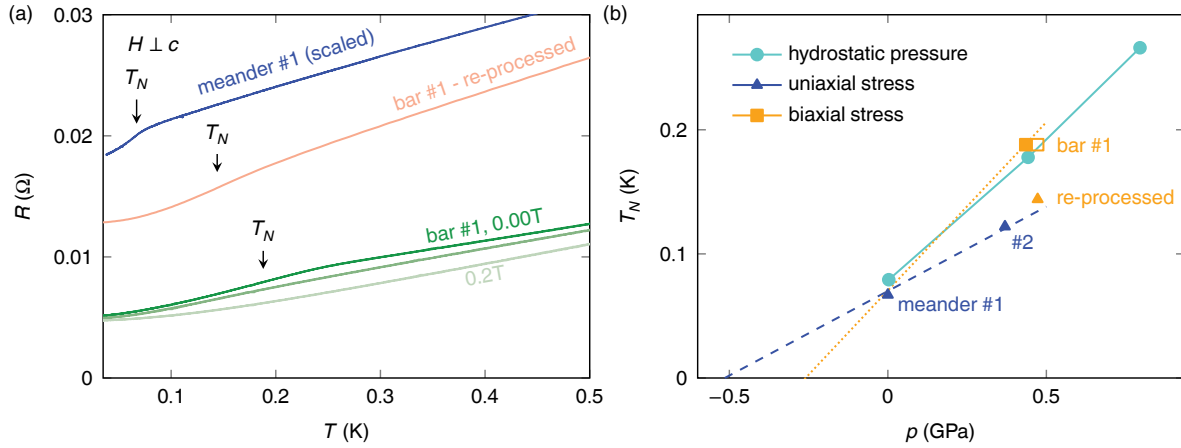


Figure 6. (a) Low-temperature resistance measurements of meander and bar samples. The difference in thermal contraction between substrate and samples leads to a shift of T_N which is geometry-dependent. Whereas in meander #1 no shift occurred, the transition into the AFM state in the bar-shaped sample onsets at about 188 mK. By partial removal of epoxy below the sample (bar #1 re-processed) this shift can be reversed. (b) Comparison of Néel transition temperatures in YbRh_2Si_2 for hydrostatic pressure [66] and uni- or biaxial stress due to differential thermal contraction in structured samples. The stress of the samples is estimated using the Ehrenfest relation and is predominantly uniaxial (dashed) in the meander samples and biaxial (dotted) in the bar #1 sample (closed symbols). Alternatively, the stress can be estimated from the differential thermal contraction (open symbol). With re-processing the stress character can be modified in bar #1 from biaxial to uniaxial.

Motivated by the significant change of T_N to higher temperatures, we can estimate which stress would be required to drive the transition temperature to zero. From equation (7) we obtain for the in-plane strain component a slope dT_N/dp_{\perp} of 0.15 K/GPa as shown in figure 6(b). To completely suppress the antiferromagnetic order we therefore

require an in-plane tensile stress between -0.5 GPa and -0.25 GPa in, respectively, the uniaxial or biaxial case, as shown in the extrapolation in figure 6(b).

The corresponding strain can be estimated from measurements of the bulk modulus B in YbRh_2Si_2 if we disregard any anisotropy of the mechanical properties. Under these assumptions and using a Poisson's ratio of $\nu \approx 1/3$ the Young's modulus $E = 3B(1 - 2\nu)$ equals the bulk modulus. With a measured room temperature value of $B = 189$ GPa [71] the corresponding uniaxial tensile strain of $\epsilon_{\perp} = -dp_{\perp}/E = -0.26\%$ is rather high and possibly beyond the elastic limit of the material. On the other hand a mismatch in thermal expansion between sample and substrate leads to a biaxial stress and, under ideal circumstances, the required strain is reduced into two equal uniaxial components of $\epsilon_{a,b} \approx -0.13\%$.

6. Ultra-low temperature noise measurements on meander #2

When designing an ultra-low temperature experiment, one has to consider the lowest temperature T_s that a metallic sample can reach, if one point of the sample is well-thermalized to the refrigerator at temperature T_0 . Electron-phonon coupling is weak at ultra-low temperatures, and typically the cooling is dominated by electrons obeying the Wiedemann-Franz law in the cooling contact and the sample, giving

$$T_s^2 - T_0^2 \approx (P_{\text{diss}} + \dot{Q}_0)(R_s + R_c)/L_0, \quad (8)$$

where in addition to the dissipation P_{diss} in the resistance measurement introduced above, we consider the spurious heat leak to the experiment \dot{Q}_0 . Here T_0 is the temperature of the refrigerator and $L_0 = 2.44 \times 10^{-8} \text{ W}\Omega/\text{K}^2$ is the Lorenz number. Details such as the position of the cooling contact within the sample and whether \dot{Q}_0 is generated uniformly within the sample, lead to prefactors of order unity in Eq. (8). For the nuclear demagnetisation refrigerator with base temperature $T_0 = 0.5$ mK, $R_s + R_c = 0.1 \Omega$, the applied power must be $P_{\text{diss}} + \dot{Q}_0 < 0.2$ pW in order to reach $T_s < 1$ mK.

The meander #2 is well-suited to ultra-low temperature experiments due to its low contact resistance, achieved by evaporating a gold film on top of the contact pads. Furthermore the pad in the middle of the meander was chosen for cooling, and this was connected to the electrical and thermal ground via two ultrasonically bonded $25 \mu\text{m}$ Au wires in parallel. At 4 K we measured 3.54Ω across the whole meander, while each half to ground was 1.56Ω and 1.98Ω . Since these numbers add up, the $10 \text{ m}\Omega$ uncertainty of these measurements gives the upper bound on contact resistance R_c , satisfying $R_c \ll R_s$.

For the initial ultra-low-temperature investigation we configured this microstructure as a SQUID-based current-sensing noise thermometer [13]. The outer contact pads of the meander were connected to Nb/NbTi leads of the SQUID current sensor with ultrasonically-bonded $25 \mu\text{m}$ Al wires. The experiment was enclosed in a Nb shield trapping Earth's magnetic field. The chosen non-dissipative technique with no direct connections to room-temperature electronics ensured $P_{\text{diss}} = 0$ and $\dot{Q}_0 < 1$ pW [13].

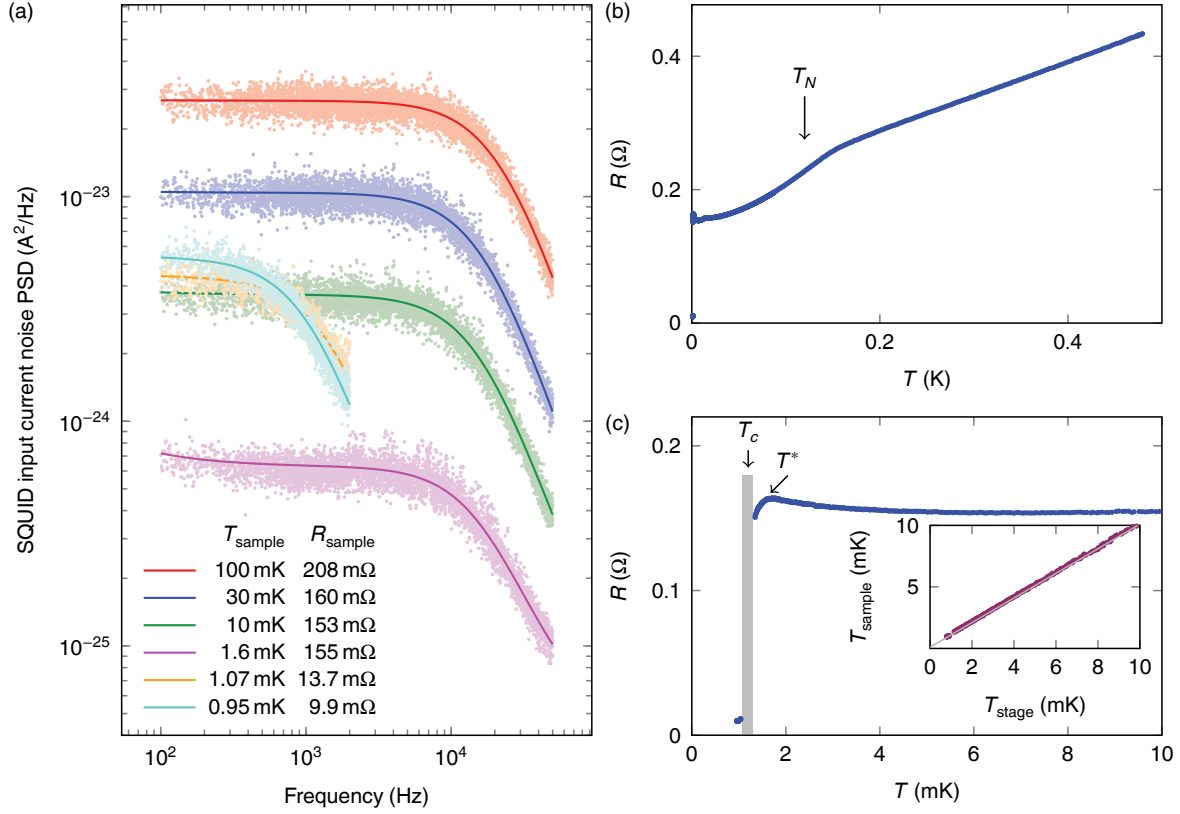


Figure 7. Noise measurements of meander #2 down to ultra-low temperatures at Earth’s field: (a) Power spectral density (PSD) of the current measured by the SQUID current sensor as a function of frequency and fits according to Eq. (9). (b) Temperature dependence of the resistance of the meander extracted from noise measurements across the AFM transition at $T_N = 120$ mK. The transition is as sharp as that measured in bulk samples (see figure 2). (c) Resistance of the meander for temperatures below 10 mK. The lowest sample temperature was 0.95 mK. The grey region indicates the temperature range $T_c = 1.2 \pm 0.1$ mK, where strong resistance fluctuations prevent reliable estimation of the sample resistance and temperature. We attribute T_c with the superconducting transition, as the resistance drops by more than an order of magnitude across this narrow temperature range, with an onset at $T^* = 1.6$ mK. The inset shows a linear plot of the sample temperature versus the stage temperature, indicating excellent thermalization of the meander down to 1 mK.

The sample temperature T_s and the resistance R , that includes the meander and the contacts to Al, were inferred from fitting the measured power spectral density (PSD) of the SQUID input current noise, figure 7(a), to

$$S_I(f) = \frac{4k_B T_s R}{R^2 + 4\pi^2 f^2 L^2} + N + N'/f, \quad (9)$$

where $L = 1.51 \mu\text{H}$ is the input inductance of the SQUID and N and N' characterise fixed background noise and are determined from noise above 100 kHz and below 100 Hz. Here $N = 4.47 \times 10^{-26} \text{ A}^2/\text{Hz}$ and $N' = 9.19 \times 10^{-24} \text{ A}^2$.

The fit results, figure 7(b), demonstrate a Néel transition at T_N between linear temperature dependence of the resistance in the non-Fermi liquid state and quadratic

in the antiferromagnetic Fermi-liquid. By comparison with conventional resistance measurements we conclude that R is dominated by the resistance of the meander. On cooling below 10 mK, figure 7(c), we observe a weak increase in the resistance just before the steep decrease with onset at $T^* = 1.6$ mK. Between 1.1 and 1.3 mK (grey area in figure 7(c)), strong resistance fluctuations were observed, and the sample resistance and temperature could not be reliably inferred. The resistance drops by more than an order of magnitude over this temperature range, therefore we associate it with the superconducting transition temperature $T_c = 1.2 \pm 0.1$ mK. The residual $R = 10$ m Ω below T_c is consistent with the U-sections of the meander, which experience different strain than the rest of the microstructure, remaining normal.

We observe that T^* is close to the temperature $T_A = 1.5$ mK of the electro-nuclear magnetic transition [22, 72], and suggests that T^* may be the resistive signature of T_A . In this scenario, the superconductivity only emerges in the uniformly-strained structure below T_A , unlike the transport signatures reported in bulk crystals at 6-8 mK [24, 25]. Alternatively, T_A may coincide with T_c , as suggested in Ref. [22], both being shifted down due to the strain that increases T_N with T^* being the onset of T_c and not a separate feature.

The sample temperature was found to be in good agreement with the temperature of the refrigerator, reaching $T_s = 0.96$ mK at $T_0 = 0.79$ mK. Estimating the heat leak \dot{Q}_0 is more straightforward in the normal state, where no strong violations of the Wiedemann-Franz law are expected. Using the observed $T_s = 1.60$ mK at $T_0 = 1.44$ mK we estimate $\dot{Q}_0 \approx 0.1$ pW from Eq. (8). Thorough shielding of the sample and filtering of the measurement lines [73] are expected to reduce \dot{Q}_0 by 1-2 orders of magnitude, opening temperatures well below 1 mK to microstructured devices and enabling driven resistance measurements, that can clearly distinguish between the sample and contact resistances.

7. Conclusion

To extract the intrinsic properties of high-quality materials by low-temperature resistance measurements remains challenging due to the trade-off between dissipation and obtained signal amplitude. With FIB microstructuring we demonstrated an increase in resistance in samples of YbRh_2Si_2 by several orders of magnitude without negatively altering their characteristics and physical properties. The sharpness of the AFM transition in resistivity at $T_N \approx 70$ mK and the onset of superconductivity below $T_c \approx 1.2$ mK, expected only for high-quality and homogeneous samples, provide strong evidence for this. Moreover, the larger resistance provides a significant increase in resolution and therefore revealed quantum oscillations signatures in resistance in fields between 13 and 18 T. This process enables noise spectroscopy measurements of metallic samples, which requires that the contact resistance becomes negligible compared to the sample resistance. Here we observe typical $1/f$ -type fluctuations in high-temperature noise spectra in a microstructured sample. By going to ultra-low temperatures, SQUID-based noise measurements demonstrate that a microstructured sample can be

cooled down below 1 mK while measuring simultaneously its intrinsic resistance and temperature. Finally, with thin and structured samples we could induce a significant shift of the Néel transition to up to 188 mK from the differential thermal expansion between samples and substrates through a thin epoxy layer. This allows for different material combinations to apply both compressive and tensile stress, with the potential to reach a stress-induced QCP in YbRh_2Si_2 . Going beyond the two-dimensional structures shown here allows detailed analysis of anisotropy effects, but also requires a more complex fabrication process which will be part of a future study [74].

Acknowledgments

The authors would like to thank A. Casey, S. Friedemann, M. Garst, P. Gegenwart, C. Geibel, R. K uchler, S. Lausberg, P. J. W. Moll, Y. Ny eki, K. Semeniuk, K. R. Shirer, F. Steglich and G. Zwicky for motivating discussions. P. Wein and C. Butzke for sample preparation and evaluation of thermal expansion data. J. M. Ellinghaus for testing the micro-milling properties of YbRh_2Si_2 (Fraunhofer IPT, Aachen, Germany) and V. Antonov (RHUL, London) for aluminium and gold wirebonds. We acknowledge funding by the German Research Foundation (DFG) via the TRR 288 (422213477, project A03, A10 and B02) and projects KR3831/4-1 and BR 4110/1-1. This work was supported by the EU H2020 European Microkelvin Platform EMP, Grant No. 824109.

8. Appendix

8.1. Microstructuring possibilities

We considered alternative microstructuring methods which including milling, electro discharge machining (EDM) or laser cutting which can be more flexible but are less suitable for this type of application.

Micromachining using milling of single crystalline materials is difficult because instead of shaving off chips from the workpiece large platelets break from the edges. In tests with YbRh_2Si_2 using a 50 μm diameter high speed steel end mill and slot widths between 100 to 200 μm were achievable, although with significant damage from the milling procedure [75]. In oxide materials such as LiNbO_3 channels with widths of 300 μm were milled using a diamond-coated bit with relatively few surface defects [76]. This approach would need to be scaled to much smaller channel widths though to achieve large resistance changes. Cutting millimeter sized bars from larger single crystals using EDM is an established technique for high purity materials, used for example to cut needles out of the unconventional superconductor UPt_3 [77]. Depending on the metallurgy and machining parameters the surface damage can be minimized but the heat affected zone where significant changes to the crystalline properties occur extends tens of microns into the material [78]. It is therefore unsuitable for small slot widths or requires additional preparation steps such as chemical etching after the machining. When using a laser to cut into a material along the edge of the cutting path melting leads

to changes of the crystalline structure. The width of this heat affected zone is comparable to that obtained by using EDM. In experiments using chromium-molybdenum steel the material properties converge to bulk properties in a depth of approximately $50 \mu\text{m}$ from the cut surface [79].

8.2. FIB structuring technique

In general, FIB-structuring can be used to pattern bulk materials into customized geometries which allow to directly access the sample properties under investigation. For example, FIB patterning has been used to prepare samples with high aspect ratios to investigate materials with very low resistivity by means of electrical transport [15] or to align the device geometry precisely with the crystalline axes to study orientation-dependent phenomena [80]. For any sample geometry, the detrimental effect on the sample material due to the exposure to ion beams can be kept at a minimum by applying an appropriate sequence of process steps, e.g. using grazing incidence in the final polishing steps. The damage to the sample such as implantation of Ga atoms and distortions to the lattice structure depends on material properties, e.g. composition, but is typically limited to a few 10 nm from the surface [81].

9. References

- [1] Kummamuru R K and Soh Y A 2008 *Nature* **452** 859–863 ISSN 1476-4687
- [2] Bartlett J M, Steppke A, Hosoi S, Noad H, Park J, Timm C, Shibauchi T, Mackenzie A P and Hicks C W 2021 *Phys. Rev. X* **11** 021038
- [3] Stutt C A 1949 Low-frequency spectrum of lock-in amplifiers Technical report 105 Massachusetts Institute of Technology, Research Laboratory of Electronics
- [4] Elmer P 2000 Specifying lock-in amplifiers Tech. rep. Technical Note TN 1001
- [5] Temple P A 1975 *Am. J. Phys.* **43** 801
- [6] Pobell F 2007 *Matter and Methods at Low Temperatures* 3rd ed (Springer Berlin Heidelberg) ISBN 3-540-46356-9
- [7] Onnes H K 1991 *Through Measurement to Knowledge* Boston Studies in the Philosophy and History of Science (Springer Netherlands)
- [8] CMR-Direct 2001 LLT-m Specifications URL http://www.cmr-direct.com/en/product/download/get?download_id=33
- [9] Drung D, Abmann C, Beyer J, Kirste A, Peters M, Ruede F and Schurig T 2007 *IEEE Trans. Appl. Supercond.* **17** 699–704
- [10] Johnson J B 1928 *Phys. Rev.* **32**(1) 97–109
- [11] Giffard R P, Webb R A and Wheatley J C 1972 *J. Low Temp. Phys.* **6** 533–610
- [12] Webb R A, Giffard R P and Wheatley J C 1973 *J. Low Temp. Phys.* **13** 383–429
- [13] Casey A, Arnold F, Levitin L V, Lusher C P, Nyéki J, Saunders J, Shibahara A, van der Vliet H, Yager B, Drung D, Schurig T, Batey G, Cuthbert M N and Matthews A J 2014 *J. Low Temp. Phys.* **175** 764–775
- [14] Moll P J W, Puzniak R, Balakirev F, Rogacki K, Karpinski J, Zhigadlo N D and Batlogg B 2010 *Nat. Mater.* **9** 628–633
- [15] Moll P J W, Kushwaha P, Nandi N, Schmidt B and Mackenzie A P 2016 *Science* **351** 1061–1064
- [16] Putzke C, Bachmann M D, McGuinness P, Zhakina E, Sunko V, Konczykowski M, Oka T, Moessner R, Stern A, König M, Khim S, Mackenzie A P and Moll P J 2020 *Science* **368** 1234–1238

- [17] Pfau H, Daou R, Friedemann S, Karbassi S, Ghannadzadeh S, Küchler R, Hamann S, Steppke A, Sun D, König M, Mackenzie A P, Kliemt K, Krellner C and Brando M 2017 Phys. Rev. Lett. **119**(12) 126402 URL <https://link.aps.org/doi/10.1103/PhysRevLett.119.126402>
- [18] Trovarelli O, Geibel C, Mederle S, Langhammer C, Grosche F M, Gegenwart P, Lang M, Sparn G and Steglich F 2000 Phys. Rev. Lett. **85** 626–629
- [19] Custers J, Gegenwart P, Wilhelm H, Neumaier K, Tokiwa Y, Trovarelli O, Geibel C, Steglich F, Pépin C and Coleman P 2003 Nature **424** 524–527
- [20] Gegenwart P, Si Q and Steglich F 2008 Nat. Phys. **4** 186–197
- [21] Gegenwart P, Westerkamp T, Krellner C, Brando M, Tokiwa Y, Geibel C and Steglich F 2008 Physica B **403** 1184–1188 ISSN 0921-4526 URL <https://www.sciencedirect.com/science/article/pii/S0921452607010897>
- [22] Schuberth E, Tippmann M, Steinke L, Lausberg S, Steppke A, Brando M, Krellner C, Geibel C, Yu R, Si Q and Steglich F 2016 Science **351** 485–488
- [23] Steinke L, Schuberth E, Lausberg S, Tippmann M, Steppke A, Krellner C, Geibel C, Steglich F and Brando M 2017 J. Phys. Conf. Ser. **807** 052007 URL <https://doi.org/10.1088/1742-6596/807/5/052007>
- [24] Nguyen D H, Sidorenko A, Taupin M, Knebel G, Lapertot G, Schuberth E and Paschen S 2021 Nat. Comm. **12** 4341 ISSN 2041-1723 URL <https://doi.org/10.1038/s41467-021-24670-z>
- [25] Levitin L V and *et al* unpublished
- [26] Nakatsuji S, Kuga K, Machida Y, Tayama T, Sakakibara T, Karaki Y, Ishimoto H, Yonezawa S, Maeno Y, Pearson E, Lonzarich G, Balicas L, Lee H and Fisk Z 2008 Nat. Phys. **4** 603
- [27] Petrovic C, Pagliuso P G, Hundley M F, Movshovich R, Sarrao J L, Thompson J D, Fisk Z and Monthoux P 2001 J. Phys. Condens. Matter **13** L337
- [28] Steglich F, Aarts J, Bredl C D, Lieke W, Meschede D, Franz W and Schäfer H 1979 Phys. Rev. Lett. **43** 1892–1896
- [29] Mathur N D, Grosche F M, Julian S R, Walker I R, Freye D M, Haselwimmer R K W and Lonzarich G G 1998 Nature **394** 39–43
- [30] Lee P A, Nagaosa N and Wen X G 2006 Rev. Mod. Phys. **78**(1) 17–85
- [31] Toyota N, Lang M and Müller J 2007 Low-Dimensional Molecular Metals Solid State Science (Springer-Verlag Berlin Heidelberg)
- [32] Kanoda K 2008 Mott transition and superconductivity in quasi-2D organic conductors, in A. Lebed (ed.) "The Physics of Organic Superconductors and Conductors" (Springer-Verlag, Berlin Heidelberg)
- [33] Krellner C, Taube S, Westerkamp T, Hossain Z and Geibel C 2012 Phil. Mag. **92** 2508
- [34] Steglich F, Pfau H, Lausberg S, Hamann S, Sun P, Stockert U, Brando M, Friedemann S, Krellner C, Geibel C, Wirth S, Kirchner S, Abrahams E and Si Q 2014 J. Phys. Soc. Jpn. **83** 061001 URL <https://doi.org/10.7566/JPSJ.83.061001>
- [35] Gegenwart P, Custers J, Geibel C, Neumaier K, Tayama T, Tenya K, Trovarelli O and Steglich F 2002 Phys. Rev. Lett. **89**(5) 056402 URL <https://link.aps.org/doi/10.1103/PhysRevLett.89.056402>
- [36] Brando M, Pedrero L, Westerkamp T, Krellner C, Gegenwart P, Geibel C and Steglich F 2013 Phys. Status Solidi B **250** 485–490 URL <https://onlinelibrary.wiley.com/doi/abs/10.1002/pssb.201200771>
- [37] Custers J 2004 Quantum-Critical Behavior in the Heavy-Fermion Compounds YbRh_2Si_2 and $\text{CeIn}_{3-x}\text{Sn}_x$ PhD thesis Technical University of Dresden, Germany
- [38] Westerkamp T 2009 Quantenphasenübergänge in den Schwere-Fermionen-Systemen $\text{Yb}(\text{Rh}_{1-x}\text{M}_x)_2\text{Si}_2$ und $\text{CePd}_{1-x}\text{Rh}_x$ PhD thesis Technical University of Dresden, Germany
- [39] Rosch A 1999 Phys. Rev. Lett. **82**(21) 4280–4283 URL <https://link.aps.org/doi/10.1103/PhysRevLett.82.4280>
- [40] Nozières P and Pines D 2018 The Theory of Quantum Liquids: Superfluid Bose Liquids (CRC Press)

- [41] Rourke P M C, McCollam A, Lapertot G, Knebel G, Flouquet J and Julian S R 2008 Phys. Rev. Lett. **101**(23) 237205 URL <https://link.aps.org/doi/10.1103/PhysRevLett.101.237205>
- [42] Zwicknagl G 2011 J. Phys. Condens. Matter **23** 094215 URL <https://doi.org/10.1088/0953-8984/23/9/094215>
- [43] Pfau H, Daou R, Lausberg S, Naren H R, Brando M, Friedemann S, Wirth S, Westerkamp T, Stockert U, Gegenwart P, Krellner C, Geibel C, Zwicknagl G and Steglich F 2013 Phys. Rev. Lett. **110** 256403 ISSN 0031-9007 URL <http://link.aps.org/doi/10.1103/PhysRevLett.110.256403>
- [44] Pourret A, Knebel G, D Matsuda T, Lapertot G and Flouquet J 2013 J. Phys. Soc. Jpn. **82** 053704 URL <https://doi.org/10.7566/JPSJ.82.053704>
- [45] Sutton A B, Rourke P M C, Taufour V, McCollam A, Lapertot G, Knebel G, Flouquet J and Julian S R 2010 Phys. Status Solidi B **247** 549–552
- [46] Pourret A, Sharapov S G, Matsuda T D, Knebel G, Zwicknagl G and Varlamov A A 2019 J. Phys. Soc. Jpn. **88** 104702 URL <https://doi.org/10.7566/JPSJ.88.104702>
- [47] Naren H R, Friedemann S, Zwicknagl G, Krellner C, Geibel C, Steglich F and Wirth S 2013 New J. Phys. **15** 093032 URL <https://doi.org/10.1088/1367-2630/15/9/093032>
- [48] Knebel G, Boursier R, Hassinger E, Lapertot G, G Niklowitz P, Pourret A, Salce B, P Sanchez J, Sheikin I, Bonville P, Harima H and Flouquet J 2006 J. Phys. Soc. Jpn. **75** 114709 URL <https://doi.org/10.1143/JPSJ.75.114709>
- [49] Friedemann S, Goh S K, Rourke P M C, Reiss P, Sutherland M L, Grosche F M, Zwicknagl G and Fisk Z 2013 New J. Phys. **15** 093014 ISSN 1367-2630
- [50] Kliemt K, Peters M, Feldmann F, Kraiker A, Tran D M, Rongstock S, Hellwig J, Witt S, Bolte M and Krellner C 2020 Crystal Research and Technology **55** 1900116 ISSN 1521-4079
- [51] Kummer K, Patil S, Chikina A, Güttler M, Höppner M, Generalov A, Danzenbächer S, Seiro S, Hannaske A, Krellner C, Kucherenko Y, Shi M, Radovic M, Rienks E, Zwicknagl G, Matho K, Allen J W, Laubschat C, Geibel C and Vyalikh D V 2015 Phys. Rev. X **5**(1) 011028 URL <https://link.aps.org/doi/10.1103/PhysRevX.5.011028>
- [52] Müller J and Thomas T 2018 Crystals **8** ISSN 2073-4352 URL <https://www.mdpi.com/2073-4352/8/4/166>
- [53] Kogan S 1996 Electronic Noise and Fluctuations in Solids cambridge, uk ed (Cambridge University Press)
- [54] Raquet B 2001 Electronic Noise in Magnetic Materials and Devices 3rd ed (Springer Berlin Heidelberg)
- [55] Müller J 2011 Chem. Phys. Chem. **12** 1222–1245
- [56] Müller J, Brandenburg J and Schlueter J A 2009 Phys. Rev. Lett. **102**(4) 047004 URL <https://link.aps.org/doi/10.1103/PhysRevLett.102.047004>
- [57] Hartmann B, Zielke D, Polzin J, Sasaki T and Müller J 2015 Phys. Rev. Lett. **114**(21) 216403 URL <https://link.aps.org/doi/10.1103/PhysRevLett.114.216403>
- [58] Sasaki S, Hashimoto K, Kobayashi R, Itoh K, Iguchi S, Nishio Y, Ikemoto Y, Moriwaki T, Yoneyama N, Watanabe M, Ueda A, Mori H, Kobayashi K, Kumai R, Murakami Y, Müller J and Sasaki T 2017 Science **357** 1381–1385
- [59] Thomas T, Saito Y, Agarmani Y, Thyzel T, Lonsky M, Hashimoto K, Sasaki T, Lang M and Müller J 2022 Phys. Rev. B **105**(4) L041114 URL <https://link.aps.org/doi/10.1103/PhysRevB.105.L041114>
- [60] Hooge F N 1969 Phys. Lett. A **29** 139–140
- [61] Scofield J 1987 Rev. Sci. Instr. **58** 985–993
- [62] Paschen S, Lühmann T, Wirth S, Gegenwart P, Trovarelli O, Geibel C, Steglich F, Coleman P and Si Q 2004 Nature **432** 881–885
- [63] Bachmann M D, Ferguson G M, Theuss F, Meng T, Putzke C, Helm T, Shirer K R, Li Y S, Modic K A, Nicklas M, König M, Low D, Ghosh S, Mackenzie A P, Arnold F, Hassinger E, McDonald R D, Winter L E, Bauer E D, Ronning F, Ramshaw B J, Nowack K C and Moll P J W 2019

- Science **366** 221–226 ISSN 0036-8075, 1095-9203
- [64] Park J, Bartlett J M, Noad H M L, Stern A L, Barber M E, König M, Hosoi S, Shibauchi T, Mackenzie A P, Steppke A and Hicks C W 2020 Rev. Sci. Instr. **91** 083902 ISSN 0034-6748
- [65] Küchler R 2005 Thermische Ausdehnung und divergierendes Grüneisenverhältnis in Schwere-Fermionen-Systemen PhD thesis Technical University of Dresden, Germany
- [66] Mederle S, Borth R, Geibel C, Grosche F M, Sparn G, Trovarelli O and Steglich F 2002 J. Phys. Condens. Matter **14** 10731–10736 ISSN 0953-8984 URL <http://iopscience.iop.org/0953-8984/14/44/367%5Cnhttp://stacks.iop.org/0953-8984/14/i=44/a=367?key=crossref.eddbd10eb0802a6a9fcc60be6ff2c7f3>
- [67] Perea-Solano B 2004 Cryogenic Silicon Microstrip Detector Modules for LHC (Barcelona: Barcelona, Polytecnic U) ISBN 978-84-688-8952-8
- [68] Kagayama T and Oomi G 1990 J. Magn. Magn. Mater. **90-91** 449–450 ISSN 0304-8853 URL <https://www.sciencedirect.com/science/article/pii/S0304885310801611>
- [69] Schmiedeshoff G M, Lounsbury A W, Luna D J, Okraku E W, Tracy S J, Bud'ko S and Canfield P C 2009 J. Phys. Conf. Ser. **150** URL <https://www.proquest.com/scholarly-journals/thermal-expansion-heavy-fermion-borocarbide-ybni/docview/2580233388/se-2?accountid=104621>
- [70] Matsumoto Y, Kuga K, Tomita T, Küchler R and Nakatsuji S 2017 J. Phys. Conf. Ser. **807** 022005 URL <https://doi.org/10.1088/1742-6596/807/2/022005>
- [71] Plessel J, Abd-Elmeguid M, Sanchez J, Knebel G, Geibel C, Trovarelli O and Steglich F 2003 Phys. Rev. B **67** 180403 ISSN 0163-1829 URL <http://link.aps.org/doi/10.1103/PhysRevB.67.180403>
- [72] Knapp J and *et al* unpublished
- [73] Levitin L V, van der Vliet H, Theisen T, Dimitriadis S, Lucas M, Corcoles A D, Nyéki J, Casey A J, Creeth G, Farrer I *et al.* 2022 Nature communications **13** 1–8
- [74] Shirer K R and *et al* unpublished
- [75] Fraunhofer Institute for Production Technology, Aachen, Germany
- [76] Huo D, Choong Z J, Shi Y, Hedley J and Zhao Y 2016 J. Micromech. Microeng. **26** 095005 ISSN 0960-1317 URL <http://stacks.iop.org/0960-1317/26/i=9/a=095005>
- [77] Kycia J B, Hong J I, Graf M J, Sauls J A, Seidman D N and Halperin W P 1998 Phys. Rev. B **58** R603–R606 URL <http://link.aps.org/doi/10.1103/PhysRevB.58.R603>
- [78] Bleys P, Kruth J P, Lauwers B, Schacht B, Balasubramanian V, Froyen L and Van Humbeeck J 2006 Adv. Eng. Mater. **8** 15–25 ISSN 1527-2648 URL <http://onlinelibrary.wiley.com/doi/10.1002/adem.200500211/abstract>
- [79] Singh R, Alberts M J and Melkote S N 2008 Int. J. Mach. Tools Manuf. **48** 994–1004 ISSN 0890-6955 URL <http://www.sciencedirect.com/science/article/pii/S0890695508000126>
- [80] Moll P J W, Balicas L, Zhu X, Wen H H, Zhigadlo N D, Karpinski J and Batlogg B 2014 Phys. Rev. Lett. **113** 186402 URL <http://link.aps.org/doi/10.1103/PhysRevLett.113.186402>
- [81] Moll P J 2018 Annual Review of Condensed Matter Physics **9** 147–162